# Fine tuning of Nb-incorporated TiO2 thin films by atomic layer deposition and application as efficient electron transport layer in perovskite solar cells

Thomas Vincent, Damien Coutancier, Pia Dally, Mirella Al Katrib, Mathieu Frégnaux, Stefania Cacovich, Frédérique Donsanti, Armelle Yaïche, Karim Medjoubi, Thomas Guillemot, et al.

# Fine tuning of Nb-incorporated $TiO_2$ thin films by ALD and application as efficient electron transport layer in perovskite solar cells

Running title: Fine tuning of Nb-incorporated $TiO_2$ thin films by ALD and application as efficient electron transport layer in perovskite solar cells

Running Authors: Vincent et al.

Thomas Vincent,[1] Damien Coutancier,[1,2] Pia Dally,[1,3] Mirella Al Katrib,[1,3] Mathieu Frégnaux,[1,3] Stefania Cacovich,[1,2] Frédérique Donsanti,[1,4] Armelle Yaïche,[1,4] Karim Medjoubi,[1] Thomas Guillemot,[1] Marion Provost,[1] Jean Rousset,[1,4] Muriel Bouttemy,[1,3] Nathanaelle Schneider[1,2,a)]

[1]Institut Photovoltaïque d'Ile-de-France (IPVF), 18 boulevard Thomas Gobert, 91120 Palaiseau, France
[2]CNRS, UMR 9006, Institut Photovoltaïque d'Ile-de-France (IPVF), 18 boulevard Thomas Gobert, 91120 Palaiseau, France
[3]Institut Lavoisier de Versailles (ILV), Université de Versailles Saint-Quentin en Yvelines, Université Paris-Saclay, CNRS, UMR 8180, 45 avenue des Etats-Unis, 78035 Versailles Cedex, France
[4]EDF R&D, IPVF, 18 boulevard Thomas Gobert, 91120 Palaiseau, France

[a)] Electronic mail: n.schneider@cnrs.fr

Access to finely tuned thin films that can act as electron transport layer (ETL) and adapt to the absorber composition and whole cell fabrication process is key to achieve efficient perovskite-based solar cells. In this study, the growth of mixed niobium-titanium oxide (Nb-$TiO_2$) thin films by atomic layer deposition (ALD) and its use to extract photogenerated electrons is reported. Films were obtained at 200°C from titanium (IV) i-propoxide (TTIP), (t-butylimido)tris(diethylamido)niobium(V) (TBTDEN), and water by introducing $Nb_2O_5$ growth cycle in a $TiO_2$ matrix. Process parameters (order of precursor introduction, cycle ratio) were optimized, the growth mechanism and the effective Nb incorporation investigated by *in situ* quartz crystal microbalance (QCM) and X-ray photoelectron spectroscopy (XPS). The composition, morphology, structural and

optoelectronic properties of the as-deposited films were determined using a variety of characterization techniques. As a result, a fine control of the film properties (between $TiO_2$ and $Nb_2O_5$ ones) could be achieved by tuning the Nb content. To allow a successful implementation in solar devices, a comprehensive annealing study under several conditions (temperatures, various atmospheres) was conducted leading to an evolution of the optical properties due to a morphological change. Ultimately, the incorporation of these 15 nm-thick films in mesoscopic perovskite solar cells (PSCs) as ETL shows an improvement of the cell performances and of their stability with increasing Nb content, in comparison of both $TiO_2$ and $Nb_2O_5$ pure compounds, reaching power conversion efficiency (PCE) up to 18.3% and a stability above 80% of its nominal value after 138 h under illumination.

# I. INTRODUCTION

In the last decade, perovskite solar cell (PSC) has attracted scientists worldwide attention,[1–3] both as single absorber solar cells and as top cell in tandem devices, reaching record values of 26.1% and of 33.9% respectively.[4] Today, upscale manufacturing and the long-term stability of PSCs remain key issues for wide-spread applications.[5,6] The stability of the perovskite photovoltaic device is strongly affected by the interfaces between the charge transport layers (electron transport layer (ETL), hole-transport layer (HTL)) and the perovskite absorber.[7] Among different charge transport layer materials, inorganic metal oxides ($TiO_2$, $SnO_2$, $NiO_x$) have demonstrated better stability in comparison to the organic counterpart (PTAA, PCBM, Spiro-OMeTAD) due to higher resilience to heat, light, and the local chemical environment.[8] A $TiO_2$ compact layer combined with a mesoporous $TiO_2$ (mp-$TiO_2$) scaffold is the most efficient candidate so far for an ETL in mesoscopic PSCs.[9] In order to optimize and adjust the ETL optoelectrical properties, doping $TiO_2$ with certain foreign elements such as $Y^{3+}$,[10] $Ta^{5+}$,[11] or $Nb^{5+}$ is a common approach to promote electron extraction. The strategy of incorporating niobium in $TiO_2$ material has been applied on ITO-free,[12] mesoscopic[13–16] and planar PSC,[14,17–19] and leads to an improvement of power conversion efficiency (PCE),[13–16,18–20] reduction of hysteresis[16,17] and stability improvement.[13,17,18] A strong electronic coupling between the charge transport layer and the perovskite for efficient interfacial charge transfer is necessary, as well as a fine tuning of the Nb-incorporation and of the layer thickness for the optimization of the film properties. Both solution-based[13,14,16,18,19] and physical vapor deposition[12] methods have been used to prepare such

Nb-$TiO_2$ nanomaterials for PSC applications. In parallel, the ALD is a powerful technique for growing oxide layers in PSC due to its relatively low deposition temperature, uniform coverage, nano-level control of the film composition and thickness and its industrial scalability.[8,21–28] ALD is an alternative to chemical vapor deposition (CVD) method, where the substrate surface is alternately exposed to the vaporized precursor fluxes, separated by purging periods to eliminate gas-phase reactions and remove reaction byproducts. The self-limited adsorption of the precursor on the substrate surface, provides indeed inherent control of the film thickness, excellent repeatability and allow deposition of conformal and pinhole-free films with superior uniformity.[29,30] Nb-incorporated $TiO_2$ thin films can be accessed by ALD from various combinations of precursors, namely $Ti(OiPr)_4$ (TTIP)/niobium(v) ethoxide (NEO)/$H_2O$,[31] $TiCl_4$/NEO/$H_2O$,[32] $Ti(OMe)_4$/NEO/$H_2O$,[33] $TiCl_4$/niobium(v) (*t*-butylimido)tris(diethylamido) (TBTDEN)/$H_2O$,[34] and $Ti(NMe_2)_4$/TBTDEN/$H_2O$).[35] While Nb-$TiO_2$ thin films prepared by ALD have been applied in catalysis[31] and thermoelectricity[32] applications there is no, to the best of our knowledge, report of its application in PSC.

In this work, we finely tune the incorporation of Nb in $TiO_2$ thin film and probe its influence on the film properties and efficiency as ETL in PSC. For this, an alternativecombination of precursors, various sequence of precursor introduction and cycle ratio are used. Their influence on thin film optical, structural and electrochemical properties is determined, and the growth mechanism is investigated by in-situ Quartz crystal Microbalance (QCM). In the mp-PSC fabrication process, the $TiO_2$ is implemented as a bilayer, with a mesoscopic film grown on top of the Nb-$TiO_2$ one,

involving a high temperature step (500°C). Thus, to ease the integration of such ALD layers in PSC but also other fabrication processes in general, the impact of various annealing conditions on the ALD-grown layers has been investigated. Finally, the compact ALD-grown layers have been successfully implemented as ETL in complete mesoscopic PSCs. A clear positive impact of the Nb incorporation on the cell is observed with an efficiency increase of 2.1 % (PCE up to 18.3 %) and an improved stability (above 80% of its nominal value after 138 hours under illumination).

# II. EXPERIMENTAL

## *A. Material Synthesis*

Thin films were prepared in a BENEQ TFS-200 ALD reactor. (*t*-butylimido)tris(diethylamido)niobium(V) ($(((CH_3CH_2)_2N)_3Nb{=}NC(CH_3)_3$, TBTDEN, min. 98%, STREM), titanium (IV) *i*-propoxide ($Ti(OiPr)_4$, TTIP, min. 98%, STREM) and deionized water were used as Nb, Ti, and O sources, respectively. All chemicals were used without further purification. Nitrogen ($N_2$, 99.9999%, Air Liquide) was used as both carrier and purging gas. TTIP and TBTDEN were heated in hot solid source systems Beneq HS300 at $T_{TTIP}$ = 85°C and $T_{TBTDEN}$ = 70°C respectively, while deionized water was kept at room temperature. Experiments were performed at $T_{dep}$ = 200°C and the pressure in the reaction chamber was kept in the range of 1 - 2 mbar. Thin films were deposited simultaneously on 2 mm-thick sodalime glass, single-polished n-doped Si (100) wafer with native oxide top layer and fluorine-doped tin oxide (FTO) on 3 mm-thick sodalime glass.

Nb-$TiO_2$ film depositions were performed with the following program: n x ($n_1$ . {$TiO_2$} + {$Nb_2O_5$}) where n is the number of supercyle and $n_1$ the number of $TiO_2$ cycles in one supercycle. The $n_1$ values of 1, 2, 5, 10 and 20 were investigated. Three precursor sequences were investigated and referred to as sequence A (TTIP pulse / $N_2$ purge / $H_2O$ pulse / $N_2$ purge / TBTDEN pulse / $N_2$ purge / $H_2O$ pulse / $N_2$ purge) ; sequence B (TTIP pulse / $N_2$ purge / $H_2O$ pulse / $N_2$ purge / $H_2O$ pulse / $N_2$ purge / TBTDEN pulse / $N_2$ purge) ; and sequence C ($H_2O$ pulse / $N_2$ purge / TTIP pulse / $N_2$ purge / TBTDEN pulse / $N_2$ purge / $H_2O$ pulse / $N_2$ purge. A titanium oxide growth cycle, *i.e.* {$TiO_2$}, is described elsewhere.[36] A niobium oxide growth cycle, *i.e.* {$Nb_2O_5$}, corresponds to {$Nb_2O_5$} = {[TBTDEN]/$N_2$/$H_2O$/$N_2$ = [1.5/0.05/0.5/2]/5/1/5 s}. "Combination" mode was chosen to ensure proper mass transport of TTIP and TBTDEN. "Combination" mode is composed of four steps ([$t_1$/$t_2$/$t_3$/$t_4$]). First, $N_2$ is injected in the precursor hot source ($t_1$), then all valves are kept closed ($t_2$), the precursor is pulsed ($t_3$). Finally, $N_2$ is injected with simultaneous precursor pulse ($t_4$).

Post-treatments were performed by annealing at various temperatures and atmospheres. Annealing treatments under ambient air were done in a Controller P 330 Nabertherm oven, at 300°C, 500°C and 600°C with a heating speed of 1.5°C/s and a plateau of 20 min at the set temperature. Annealing treatments under $N_2$ were done in a Jipelec Jetfirst oven, at 300°C, 500°C and 600°C with the same heating sequence. Annealing treatments under forming gas (FG, 95% $N_2$ - 5% $H_2$, Alphagaz 2 quality) were done in AsOne Annealsys oven, at 400°C, 500°C and 600°C, with a heating ramp of few minutes and a plateau of 20 min.

## B. Material Characterization

Thin films were characterized on samples deposited on single-polished n-doped Si (100) wafers with native oxide layer on top (ellipsometry, GIXRD, XRR, XPS), sodalime glass (spectrophotometry) or FTO (cyclovoltammetry). Thin film thicknesses were determined by spectroscopic ellipsometry (SE) performed with a Horiba Jobin Yvon Uvisel 2 ellipsometer, and X-ray reflectivity (XRR) using a PANalytical Empyrean equipment using Cu-Kα radiations. The film thickness homogeneity was confirmed over the whole substrate area (15 x 15 $cm^2$). SE measurements in the wavelength range of 200-1700 nm were modelled using Tauc-Lorentz oscillators functions. X-ray diffraction (XRD) studies were performed under grazing incidence (GIXRD) conditions for crystallinity determination and phase detection.

Thin film compositions were obtained using a XPS Thermo Scientific K-Alpha$^+$ spectrometer equipped with a monochromated Al-Kα X-ray source for excitation at 1486.6 eV and using an X-ray spot size of 400 μm. Calibration of the spectrometer was done using Cu and Au samples following the ASTM-E-902-94 protocol. In complement to surface analyses, in-depth profiling was carried out using a monoatomic ion gun ($Ar^+$) with an energy of 1000 eV, a 10 mA current intensity and an ion gun orientation of 30° from the sample surface. The Thermo Scientific Advantage© software and library were used for the XPS data treatment and peak fitting. C 1s peak positioned at 284.9 eV was taken as a reference to present the high energy resolution core level spectra of the other elements. The valence band structure has been investigated by UPS analyses conducted on Thermo Scientific 250 Xi spectrometer with He source providing $He^I$ photons at 21.2 eV.

Transmittance and reflectance spectra were obtained using an Agilent Cary 500 UV-Vis-NIR spectrophotometer equipped with an Agilent Diffuse Reflectance accessory. Cyclovoltammetry measurements were carried out on a ALD-film/FTO/glass stack and performed with an EC-LAB SP150 Bio-logic potentiostat using 0.8-1 $cm^2$ as effective area. All films were too resistive to be characterized by four-point probe or Hall effect measurements. A classical three-electrode set up has been used with a glass/FTO substrate covered by the ALD-film as working electrode, a Pt wire as counter electrode and a saturated calomel electrode (SCE) as reference electrode ($E_{vs\ SHE}$ = 0.241 V). Thin films were dipped in a $Fe(CN)_6^{3-}$ (0.1 M) / $Fe(CN)_6^{4-}$ (0.1 M) electrolyte. For each sample, the current response was recorded during three potential cycles applied (range between +1.5 V and -1.5 V, rate = 20 mV/s).

## *C. Solar cell device fabrication and characterization*

The NIP architecture perovskite solar cells (PSCs) were fabricated with the following stack : glass substrate, FTO, niobium-incorporated titanium dioxide (Nb-$TiO_2$), mesoporous titanium dioxide (mp-$TiO_2$), triple-cation perovskite absorber ($Cs_{0,05}(MA_{0,167}FA_{0,833})_{0,95}Pb(I_{0,842}Br_{0,158})_3$, poly(triarylamine) (PTAA) HTL and Au back electrode. Description of all fabrication steps and characterization data of the perovskite absorber are provided in Supporting Information (Figures S13, S14 and S15).

**Characterization:** The current-voltage characterizations (J-V) were performed with an Oriel solar simulator under 1000 W/m² corresponding to AM1.5G spectrum at 25°C on PSC that were first light-soaked at Voc for 20 s. The irradiance was calibrated

using a Si cell with a KG5 filter, which spectral response is comparable to the one of PSCs. The scan is conducted in both directions, forward then reverse, with a rate of 20 mV/s and a voltage step of 20 mV. The min and max voltage values were set at -0.1V and +1.2V, respectively, along with an auto detect Voc, *ie* stopping the measurement just after the Voc. A rectangular mask with area of 0.09 $cm^2$ was used during the measurement to control the illuminated area. The external quantum efficiency (EQE) was measured with an Oriel IQE2000 with a step of 20 nm. Indoor accelerated ageing was conducted for 138 hours under LED solar simulator which spectrum matches to the AM1.5G (including UV portion) in a climate chamber kept under $N_2$ atmosphere at 20°C. An MPPT is conducted all along the ageing process and I-V characterizations were recorded every 15 min following the protocol described above. This experimental set-up corresponds to ISOS-L1 protocol defined in the consensus statement for PSCs reliability testing.[37]

# III. RESULTS AND DISCUSSION

A control of the Nb-incorporation, *ie* its atomic amount and dilution, is required to finely tune the properties of the thin films. By ALD, this is usually achieved by a so-called supercycle strategy, which is the combination of growth cycles of binary materials, the right combination of precursors, and the order of introduction of the precursors that directly impacts the surface chemical reactions involved.

## *A. Impact of the ALD precursor introduction sequence on Nb incorporation*

First, three precursor sequences (A, B and C, described in FIG. 1) have been tested as these are known to impact the incorporation of the additional atom.[36,38–40] Mass variations relying on molecule desorption and adsorption during the film deposition have been evidenced by recording *in situ* QCM measurements. The results obtained for the three sequences are presented in FIG. 1 and compared to the ones of pure $TiO_2$ and $Nb_2O_5$ thin films.

For those two latter, positive mass variations are recorded after each metallic precursor pulses ($\Delta m_{TiO2}^{1} = 0.85$ a.u. after TTIP pulse, and $\Delta m_{Nb2O5}^{1} = 0.82$ a.u. after TBTDEN pulse), while the $H_2O$ pulse leads to a negative mass variation ($\Delta m_{TiO2}^{2} = -0.4$ a.u. , and $\Delta m_{Nb2O5}^{2} = -0.25$ a.u.). It results in a growth per cycle (GPC) of $\Delta m_{TiO2}^{0} = 0.45$ a.u./cycle for $TiO_2$ and $\Delta m_{Nb2O5}^{0} = 0.57$ a.u./cycle for $Nb_2O_5$. Mass variations that occur during the $\{Nb_2O_5\}$ cycle introduction in $TiO_2$ were recorded for $n_1 = 5$. In case of sequence A where a water pulse follows each TTIP or TBTDEN pulse, mass variations are similar to the ones observed for pure $TiO_2$ and $Nb_2O_5$ ($\Delta m_A^{TiO2} = 0.47$ a.u./cycle and $\Delta m_A^{Nb2O5} = 0.54$ a.u./cycle). It shows that both $TiO_2$ and $Nb_2O_5$ are growing indifferently on themselves or on the other. In other words, both TTIP and TBTDEN are reacting in a very similar way on Ti-OH and Nb-OH terminated surfaces. In case of sequence B, the TBTDEN pulse is followed by a TTIP pulse. While the mass variation during TBTDEN pulse remains unchanged ($\Delta m_B^{Nb} = 0.81$ a.u.), mass variation during the TTIP pulse is significantly smaller than in sequence A ($\Delta m_B^{Ti} = 0.35$ a.u. instead of $\Delta m_{TiO2}^{1} = 0.85$ a.u.). This means that TTIP is reacting either with the Nb-ligand terminated surface fragments, or with the remaining -OH groups, or both. Finally, sequence C involves a TTIP pulse followed by a TBTDEN pulse. The TBTDEN pulse leads to no change in the

mass variation ($\Delta m_C^{Nb} \sim 0$), which shows that TBTDEN almost does not react with the TTIP-saturated surface, and makes sequence C irrelevant for incorporation of Nb in $TiO_2$.

In summary, different Nb insertion levels can be achieved by choosing the precursor sequences. Sequence C leads to little to no insertion of niobium atoms. Sequence B shows smaller growth per supercycle due to the poor reaction of TTIP on TBTDEN-saturated surfaces. For both sequences B and C, reaction mechanisms of the two successive metallic pulses cannot be fully elucidated by QCM measurements, while sequence A leads to well-described growth mechanisms similar to the ones of bare $TiO_2$ and $Nb_2O_5$. These observations, and the relative low GPC of $TiO_2$ and $Nb_2O_5$ that should prevent the formation of biphasic systems, suggest that the Nb incorporation can be more easily tuned with sequence A by adjusting the cycle ratio $n_1$.

QCM measurements were recorded with sequence A for several $n_1$ values ($n_1$ = 1, 2, 5, 10 and 20). No influence is observed on neither the $Nb_2O_5$ cycle nor the growth of $TiO_2$ cycles, which confirms the independence of the growth of the two oxides on each other (see in Supporting Information, Figure S1). Hence, sequence A was selected as the most appropriate one to finely incorporate Nb and will be used for the rest of this work.

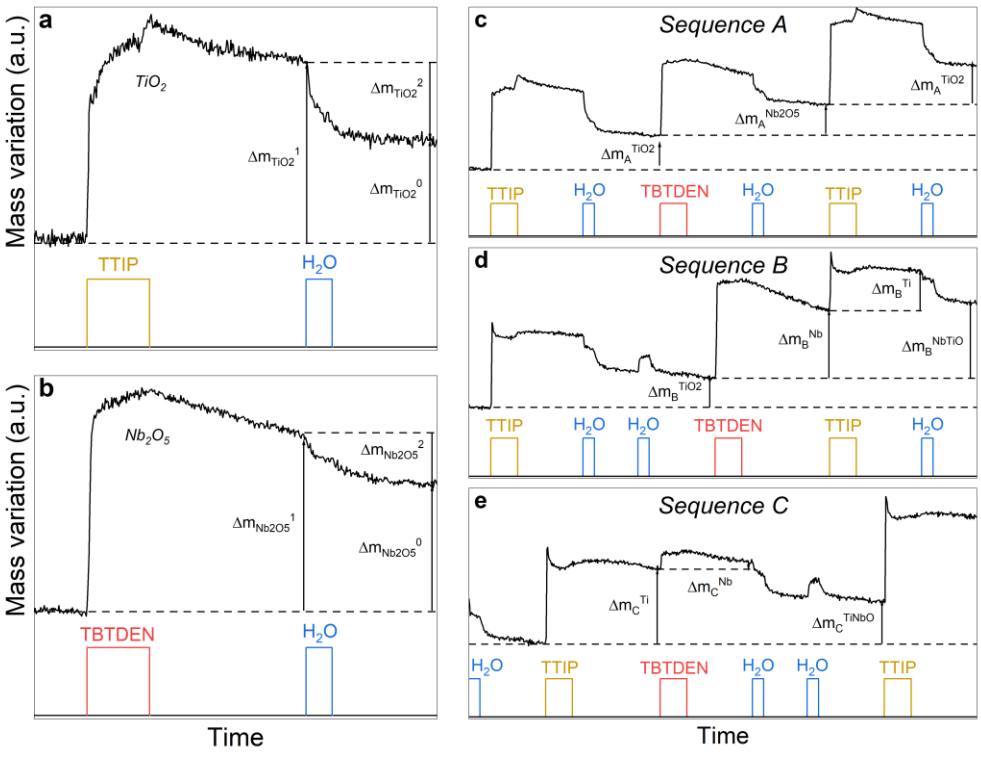


FIG. 1. Mass variations recorded by *in situ* QCM measurements for $TiO_2$ (**a**), $Nb_2O_5$ (**b**) and the three precursor sequences A (**c**), B (**d**), and C (**e**). The pulse times are depicted in colored bands below the curves.

## *B. Tuning of Nb-incorporation in $TiO_2$, influence on thin film properties and impact of post-treatments*

### *1. Tuning of Nb incorporation level and influence on thin film properties*

Using a supercycle strategy, the cycle ratio $\{TiO_2\}:\{Nb_2O_5\}$ modulates the atomic composition of the films.[41] Films with sequence A and different cycle ratios ($n_1$ = 1, 2, 5, 10, 20 *i.e.* $\{TiO_2\}:\{Nb_2O_5\}$ = (1, 2, 5, 10, 20):1) were prepared. The number of

supercycle, n, was set to generate 15 nm-thick films, considering the target application of those films as ETL in PSC. Assuming a simple rule of mixture between $TiO_2$ and $Nb_2O_5$, it corresponds to 450 cycles for $TiO_2$, 350 cycles for $Nb_2O_5$, and $\{n, n_1\} = \{200,1\}$, $\{140,2\}$, $\{72,5\}$, $\{40,10\}$, $\{20,20\}$ for Nb-incorporated $TiO_2$ thin films.

Final film thicknesses follow a simple rule of mixture, with intermediary GPC values for all Nb-$TiO_2$ samples (see Supporting Information, Figure S2). It confirms the previous hypothesis, *ie* the independence of the growth of the two oxides on each other, which lead to a simple rule of mixture. XPS measurements were performed on two points of each sample and confirmed the expected homogeneity of the surface composition and the presence of all expected elements (Ti, Nb, O) along with superficial C (13-16 at.%) and N (0.6-1.7 at.%) contaminations (see Supporting Information, Figure S3, Table S1). High energy resolution core level spectra of Ti 2p, Nb 3d, O 1s, C 1s and N 1s were recorded for all cycle ratios. Ti and Nb exhibit oxidation numbers of Ti (+IV) with binding energies (BE) of 458.6 eV ($2p_{3/2}$) and 464.5 eV ($2p_{1/2}$); and Nb (+V) with BE of 207.3 eV ($3d_{5/2}$) and 210.0 eV ($3d_{3/2}$) (FIG. 2).[35] The only significant modification observed with the cycle number variation is the relative intensity of Ti 2p and Nb 3d peaks, assessing the presence of a unique phase of $Ti_{1-x}Nb_xO_2$. The corresponding atomic percentages of Nb and Ti are then employed to calculate the doping fraction $x_{Nb}$, defined as $x_{Nb} = \frac{[Nb]}{[Nb]+[Ti]}$. FIG. 2 presents the $x_{Nb}$ fraction variation with respect to the dopant cycle ratio, defined as $R = 1/(n_1 + 1)$. We can observe that $x_{Nb}$ follows the rule of mixture (dashed line), confirming our hypothesis that both $Nb_2O_5$ and $TiO_2$ grow the same way on top of each other than on themselves. As a consequence, we demonstrated that the Nb

amount can be finely controlled by the cycle ratio in the ALD supercycle, from [Nb]/[Ti] = 0.05 ($n_1$ = 20) to 0.76 ($n_1$ = 1). A specific double structure is observed for the N contamination with two features (BE = 400.4 eV, 394.8 eV) attributed to remaining ligand fragments. The low energy feature decreases with the cycle ratio, suggesting it is due to the TBTDEN ligands while the high energy one remains constant. Despite the sputtering artefact leading to the reduction of both Nb and Ti in Nb(+IV) and Ti(+III), a constant composition is measured within the whole layer (see Supporting Information, Figure S4). Since the film thickness (15 nm) is within the range of the escape depth of photoelectrons (7-10 nm), almost the entire layer is probed at once before starting the profile. It is thus impossible to argue for a layered structure or a homogeneous one. The same conclusion rises from additional non-destructive profiling by angle-resolved measurements (from 20° to 60°) (see Supporting Information, Figure S5) where no drastic evolution of the composition is measured when probing either 2-3 nm or 7-10 nm. UPS measurements reveal an impact of the incorporation of Nb on the thin film electronic structure. Indeed, there is a shift of the Valance Band Maximum (VBM) position and of the work function, which translates in a modification of the Conduction Band Minimum (CBM) (see Supporting Information, Figure S6).

Structurally, all thin films appear amorphous as determined by GIXRD. The cycle ratio seems to have the expected impact on the optical properties of the films, namely the optical band gaps of the ALD layers are evolving continuously between the bandgap of $TiO_2$ $E_g$ = 3.32 eV and the one of $Nb_2O_5$ $E_g$ = 3.46 eV.[42,43] Cyclovoltammetry studies show that all samples are n-type (presence of a reduction peak) and display a hole-

blocking behaviour (no oxidation peak),[44] with very little impact of the Nb amount (see in Supporting Information, Figures S7, S8, S9 and S10).

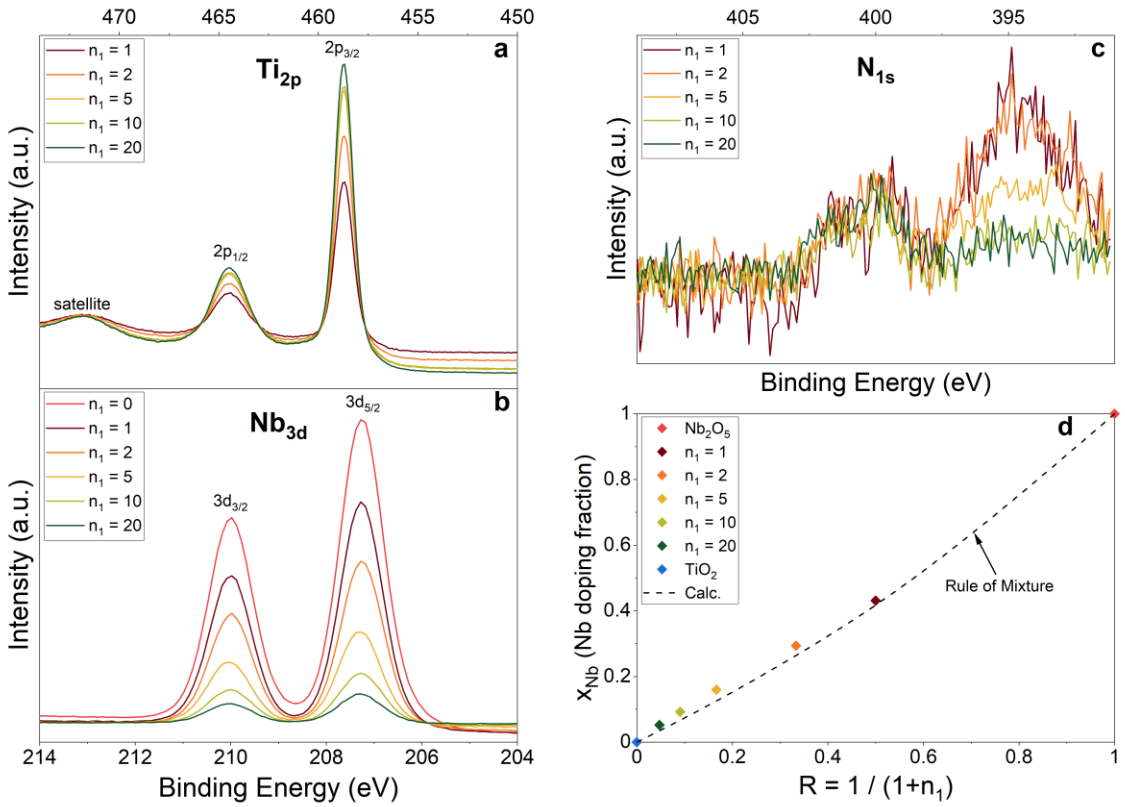


FIG. 2. XPS measurements of the Ti 2p (**a**), Nb 3d (**b**) and N 1s (**c**) peaks of Nb-incorporated $TiO_2$ samples for $n_1$ = 0, 1, 2, 5, 10, 20. The evolution of the Nb doping fraction $x_{Nb}$ calculated from the atomic percentage measured by XPS is depicted with respect to the dopant cycle ratio R (**d**).

## 2. *Impact of post-treatments on thin film properties*

In the target application, the Nb-$TiO_2$ thin films are covered with mp-$TiO_2$, which fabrication requires a heating step at 500°C under air. Hence, the influence of post-treatment on the film properties had to be investigated. More generally, as the application of those films is not limited to a single specific PSC architecture, the impact of various

annealing post-treatments, *ie* at various temperatures and atmospheres, was investigated. In particular, the impact of annealing in ambient air at 300, 500 and 600°C; in $N_2$ at 300, 500 and 600°C; and in forming gas (FG, $H_2$ 5% - $N_2$ 95%) at 400, 500, 600°C, was explored.

A first impact of annealing is evidenced by GIXRD (see in Supporting Information, Figure S10). The $TiO_2$ layer, amorphous as deposited at 200°C, crystallises at 300°C in all atmosphere conditions tested in the anatase phase (ICDD 00-021-1272), with the specific main diffraction peaks (101), (004), (200). When Nb is incorporated, the crystallization leads to the same anatase phase as $TiO_2$, for all Nb doping fraction investigated, from $x_{Nb} = 0.04$ ($n_1 = 20$) up to $x_{Nb} = 0.43$ ($n_1 = 1$). For $n_1 = 5, 10, 20$, the Nb-$TiO_2$ crystallizes at 300°C in all atmospheres. Higher amounts of Nb atoms delay the crystallization that takes place at higher temperatures (at 400°C (FG)- 500°C (air and $N_2$) for $n_1 = 2$, at 600°C in all atmospheres for $n_1 = 1$). A finer analysis shows a small shift towards lower angles of the anatase peaks for increasing Nb amount. It demonstrates an expansion of the unit cell, with a linear increase of its volume with respect to the Nb doping fraction.[32]

Electrochemical characterization by cyclovoltammetry was made for the samples annealed at 500°C. After annealing at 500°C, all samples lose their hole-blocking behaviour with the emergence of an oxidation peak (~ 1 mA after annealing in forming gas and ~0.2 mA in air), while the reduction peaks remain (see in Supporting Information, Figure S11). This can be attributed to the crystallisation of the thin films, which is accompanied by its shrinkage and the apparition of cracks and grain boundaries, as seen by scanning electron microscopy (SEM) (see Supporting Information, Figure

S12). SE and spectrophotometry measurements show a strong influence of the crystallization on the optical properties of the samples, especially on the band gap width as shown in FIG. 3. We observe an increase of 0.13 eV of the bandgap after the crystallization in the anatase phase. A smaller effect evidenced is the slight increase of the band gap with respect to the annealing temperature. At 500°C, the temperature which would be reached during the integration in the solar cell, amorphous samples reach an average bandgap of $E_g$ = 3.36 eV while the crystalline samples exhibit an average band gap of $E_g$ = 3.50 eV. The continuous evolution of the bandgap between the value of $TiO_2$ and the one of $Nb_2O_5$ with increasing Nb amount is kept for all annealing temperatures.

Such differences could lead to significant effect on solar cell performance. Hence, the five Ti:Nb ratios ($n_1$ = 1, 2, 5, 10, 20) along with the $TiO_2$ and $Nb_2O_5$ references were then integrated as ETL in perovskite solar cells, and their performances were investigated in terms of efficiency and stability.

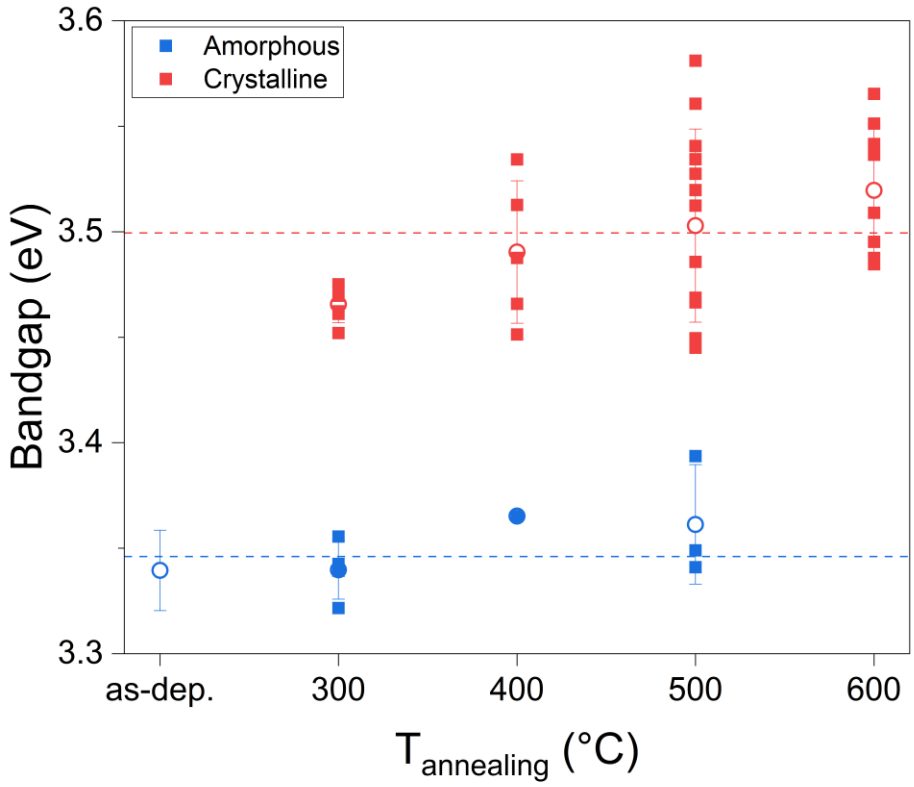


FIG. 3. Evolution of the band gap determined by SE with respect to the annealing temperature gathering the data obtained for all tested annealing atmospheres (air, $N_2$, FG). Data is plot depending on the structural properties (amorphous, blue; crystalline, red) with no regard of the Nb doping fraction or the annealing atmosphere conditions.

## C. Application of Nb-incorporated $TiO_2$ thin films by ALD as ETL in perovskite solar cells

Perovskite-based solar cells incorporating ALD-grown Nb-$TiO_2$ layers ($n_1$ = 1, 2, 5, 10 and 20) as ETL were fabricated (see schematic representation of the full stack in FIG. 4), along with devices based on bare $TiO_2$ as reference, but also bare $Nb_2O_5$ as this latter has been reported as efficient ETL for PSC.[45–47] For each condition, 4 cells were prepared and characterized by J-V measurements in both directions forward (FW) and reverse (RV), external quantum efficiency, MPPT tracking during indoor accelerated ageing under continuous illumination to evaluate their relative power conversion efficiencies and stabilities.

An important hysteresis between FW and RV measurements is observed for all samples with an average PCE difference of 3.1 % (and a relative difference $\frac{PCE_{RV}-PCE_{FW}}{PCE_{RV}} = 18.2$ %), which is common for fresh PSC (measurement at D0). In the following, we focus on RV measurements that show the best performances. First, when comparing at D0 PSC with bare $TiO_2$ or bare $Nb_2O_5$ (respectively blue and red in FIG. 4), only a slight increase of performance is observed: average PCE is 16.2 % for $TiO_2$ and 16.45 % for $Nb_2O_5$, with similar $J_{SC}$ and $V_{OC}$ values, which is accordance with the literature.[48] For all PSC with Nb-$TiO_2$ layers, a continuous increase of PCE is observed from the $TiO_2$ value up to $n_1$ = 1 with an average PCE of 17.96 % and a champion cell at 18.30 %. The open-circuit voltage $V_{OC}$ shows an increase with the Nb amount, recovering the value of both bare $TiO_2$ and $Nb_2O_5$ for $n_1$ = 1 and 2 around 1.10 V. The short-circuit current $J_{SC}$ also

exhibits an increase from 20.88 mA/cm² for $TiO_2$ to 21.98 mA/cm² for $n_1 = 1$. The fill factor (FF) shows no clear trend, although the best values are obtained for Nb-$TiO_2$ cells ($n_1 = 10$, 5 and 1) with FF values above 75 %.

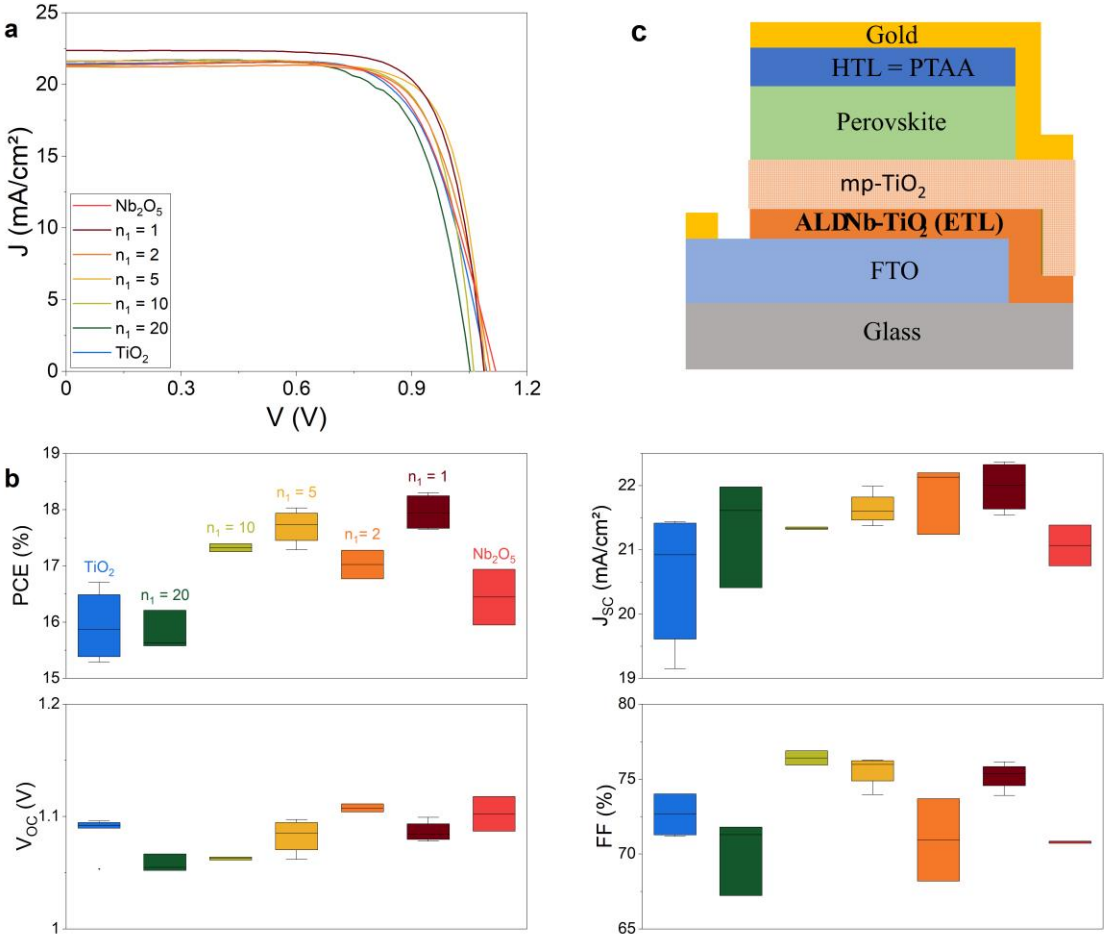


FIG. 4. J(V) (**a**) and solar cell performance characteristics (PCE, $J_{SC}$, $V_{OC}$ and FF, **b**) of PSC with various ETL compositions. Schematic representation of the complete stack of PSC (**c**).

To investigate the impact of those newly developed ETL layers on the PSC stability, two different methods were employed to determine the evolution with time of the solar cell performances.

The first common method to study ageing of PSC is referred as shelf ageing: PSC are stored in the dark and under vacuum for several days and J(V) characteristics are measured. In our case, PSC performances were determined at day 0, day 10, day 17 and day 61. FIG. 5 shows the results between at day 0 and day 61 for $TiO_2$, $n_1$ = 10, 5 and 1. Hysteresis for PCE between FW and RV measurements after 61 days disappears. PCE decays with time for all samples, although the incorporation of niobium appears to stabilize the cell. Indeed, average PCE of $TiO_2$ drops to 14.96 % while the one of $n_1$ = 1 remains at 17.55 %, with a champion cell at 18.2 %. For the PSC with the composition $n_1$ = 1, there is no hysteresis after 61 days. Moreover, the J(V) curves after 61 days are very similar to the RV curve at day 0, showing a good stability over time.

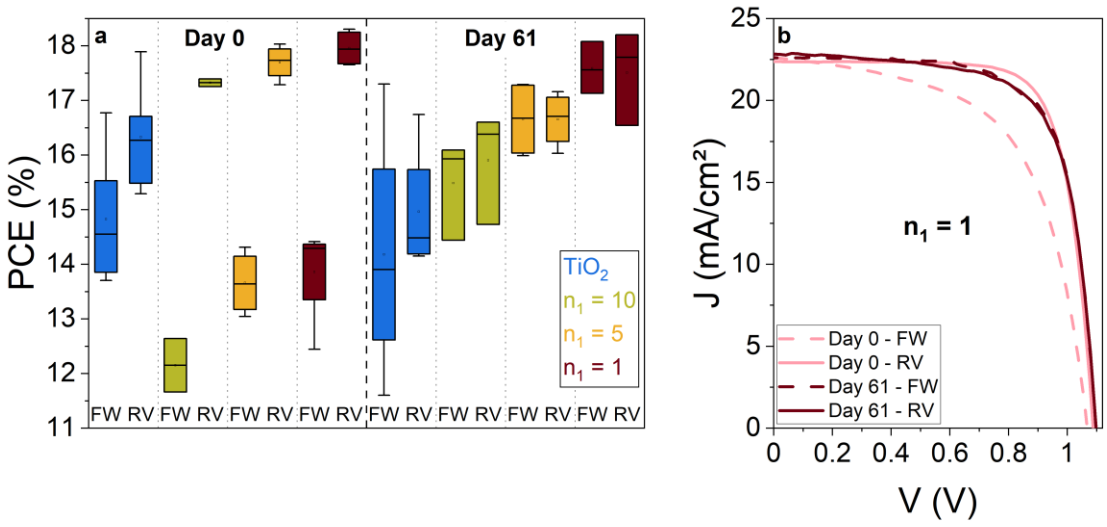


FIG. 5. Evolution of PCE for both FW and RV measurements at day 0 and day 61 of PSC with bare $TiO_2$ and Nb-$TiO_2$ with $n_1$ = 10, 5 and 1 (**a**). FW and RV J(V) curves for $n_1$ = 1 measured at day 0 and day 61 (**b**).

The second ageing method that corresponds to ISOS-L1 protocol defined in the consensus statement for PSCs reliability testing,[37] is under continuous illumination for

138 h, maximum power point tracking (MPPT) and J-V measurements taken every 15 min. This protocol was applied on PSC with pure $TiO_2$ for reference, $n_1$ values of 20 and 2, and pure $Nb_2O_5$. EQE were measured both before (beginning of the life, BOL) and after (end of life, EOL) the ageing (FIG. 6).

Device based on pure $TiO_2$ exhibit a quick loss of performance reaching 80 % of its nominal PCE value within 10 h and showing no sign of stabilization, reaching 55 % after 138 h (see FIG. 6**d**). All the cell parameters ($J_{SC}$, $V_{OC}$ and FF) present similar decreasing trends, reaching $J_{SC}$ = 81 %, $V_{OC}$ = 87 % and FF = 78 % of their nominal values after 138 h. Pure $Nb_2O_5$-based PSC efficiency shows an even faster deterioration within short ageing period, reaching 80 % after 3.5 h and 64 % after 16 h. However, after 16 hours the performances increase and stabilize above 70 % from 62 h up to 138 h under illumination, assessing a better stability than $TiO_2$ references. The PSC with Nb-$TiO_2$ layers show an intermediary behaviour. For $n_1$ = 20 (low Nb content), the deterioration seems to be slower than for pure $TiO_2$ for the first 15 hours. However, it exhibits a continuous decrease, to finally reach similar performances than $TiO_2$ after 138 hours (58 %). Finally, for $n_1$ = 2 (high Nb content) PCE is stabilised after 8 h at 77 % and slightly recovers to remain stable around 80 % of its nominal value up to 138 hours. This evidences a better stability of those cells compared to $Nb_2O_5$ ones and suggests the existence of an optimal Nb content for PSC stability. After the initial strong decrease, which is commonly attributed to interfaces,[49] the degradation rate can evaluated by a linear fit between 20 and 70 hours. In that case, PSC with pure $TiO_2$ and $n_1$ = 20 show a strong degradation with negative rates (-0.2 and -0.32 %/h respectively) while PSC with $n_1$ = 2 and $Nb_2O_5$ exhibit positive rates *i.e.* recovery (+0.01 and +0.13 %/h respectively).

The evolution of $J_{SC}$ shows a huge drop for PSC with pure $TiO_2$ (80 % of its nominal value after 138 h) while other samples remain above 90 % with a record value of 96 % for $n_1 = 2$. $V_{OC}$ and FF also show a recovery followed by a stabilization after an initial decrease for films with high Nb contents ($n_1 = 2$ and $Nb_2O_5$) and a continuous degradation for low-Nb content ($TiO_2$, $n_1 = 20$). Improved stability with Nb incorporation is confirmed by EQE measurements before (BOL) and after (EOL) 138 hours of illumination. PSC with pure $TiO_2$ or $Nb_2O_5$ layers suffer loss in EQE around 20 % and 13 % respectively, while PSC with Nb-$TiO_2$ ($n_1 = 2$) loses only 8 % and remains near 80 %.

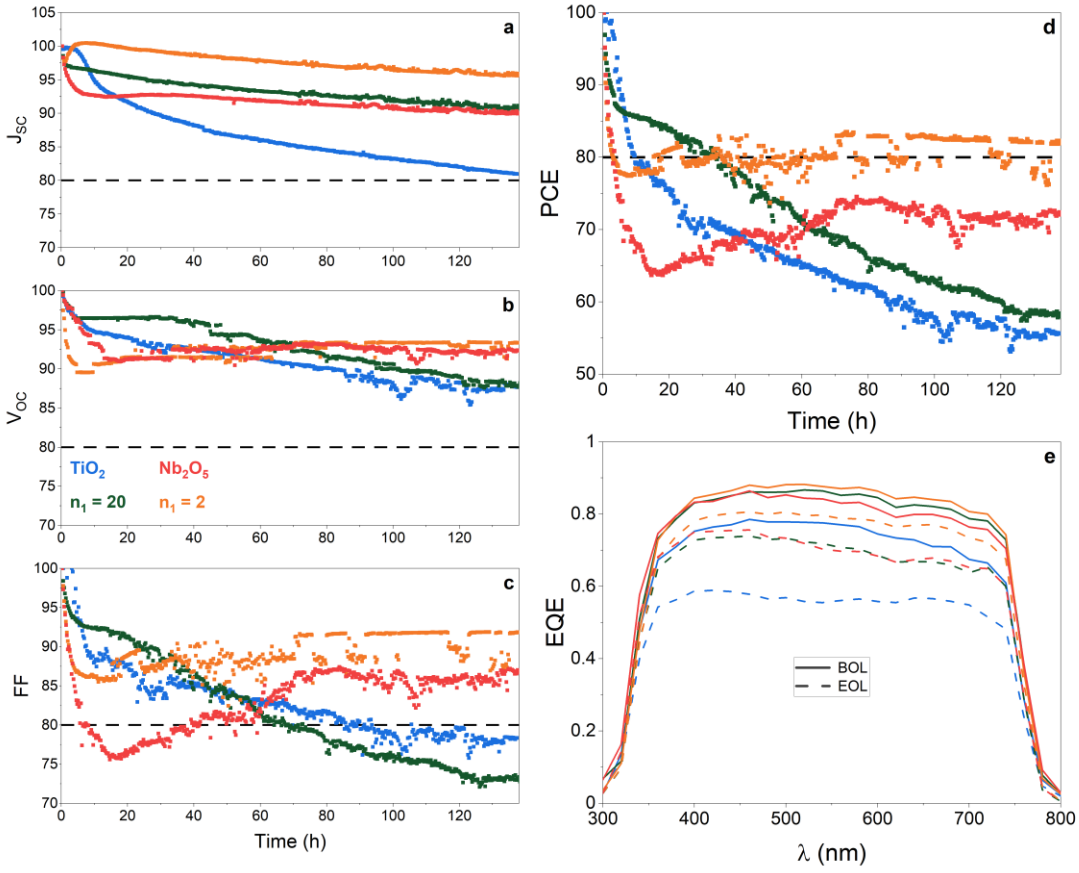


FIG. 6. Evolution of normalized PV parameters ($J_{SC}$ **a**, $V_{OC}$ **b**, FF **c** and PCE **d**) with time under constant illumination and MPPT of PSC with bare $TiO_2$, bare $Nb_2O_5$ and Nb-$TiO_2$

with $n_1$ = 2, 20. Measurements were done every 15 min; EQE measurements at BOL and EOL (**e**).

# IV. SUMMARY AND CONCLUSIONS

In summary, ALD at 200°C has been successfully used to grow Nb-$TiO_2$ thin films with a very fine tuning of the film properties. In-situ QCM measurements show that both $TiO_2$ and $Nb_2O_5$ have stable GPC values (0.47 a.u./cycle and 0.54 a.u./cycle respectively) when grown either on top of themselves or on top of one another. It allows a fine control of the film composition and thickness, which are critical for tuning film properties. Film thickness and incorporation level of Nb are confirmed by ex situ ellipsometry, XRR and XPS measurements. The homogeneity both in-depth and on the surface of the samples is insured as confirmed by multiple points, high resolution and angle-resolved XPS, along with the presence of a single amorphous phase with very low contamination.

All films remain too resistive for Hall effect measurements, but the Nb incorporation modifies the film electronic band structure as shown by UPS measurements. Films display a hole-blocking behavior and appear appropriate for an application as ETL in mesoscopic PSC. To mimic the PSC fabrication process, films were annealed at 500°C. It leads to a crystallization in the anatase phase, an increase of the bandgap of 0.13 eV and a minimal loss of the hole-blocking behavior.

When integrated as ETL in mesoscopic PSCs, the Nb-$TiO_2$ films demonstrate a continuous enhancement of the cell performances with respect to the Nb amount, up to +7 % of the $TiO_2$ value for $n_1$ =1, reaching a PCE of 18.3 %. More importantly, the

stability of the PSCs is largely improved by the incorporation of Nb. Indeed, 80% of PSC PCE nominal value is conserved after 138 hours under illumination for cell with Nb-$TiO_2$ layer ($n_1 = 2$), to be compared with 55 % for $TiO_2$ reference.

The improvement of both performance and stability of PSCs by the incorporation of Nb in a $TiO_2$ layer grown by ALD in soft conditions represents a very promising result, considering that ALD can easily be implemented in large area systems.

## SUPPLEMENTAL MATERIAL

See supplementary material at [URL will be inserted by AIP Publishing] for additional data on substrate preparation, in-situ QCM measurements (experimental details, mass variations during Nb-$TiO_2$ film growth (precursor sequence A, various $n_1$ values), characterizations of as-deposited (GPC measured by XRR and SE, surface homogeneity assessment by XPS, XPS depth profiling, angle-resolved XPS measurements, transmission- reflection measured by spectrophotometry, light absorption spectra, SE data and evolution of the optical bandgap, cyclovoltammetry) and annealed (GIXRD diffractograms, cyclovoltammetry, SEM) thin films, and solar cells (description of all fabrication steps, structural characterization of the perovskite absorber by SEM, XRD, UV-Vis absorption spectra of the stacks).

## ACKNOWLEDGMENTS

The authors would like to thank J. Cardin, C. Labbe and G. D. Gesesse (CIMAP, UMR6252, Caen, France) for their assistance in fitting SE data. This work was supported by the French Government in the frame of the program of investment for the future (Programme d'Investissement d'Avenir ANR-IEED-002-01), and the French Agence Nationale de la Recherche under the contract numbers HANAMI ANR-17-CE09-0022.

# AUTHOR DECLARATIONS

### Conflicts of Interest

The authors have no conflicts to disclose.

### Author Contributions

**Thomas Vincent** - Conceptualization (equal); Data curation (equal); Formal analysis (equal); Investigation (equal); Methodology (equal); Validation (equal);Visualization (equal); Writing – original draft (lead); Writing – review & editing (equal)

**Damien Coutancier** - Conceptualization (equal); Data curation (equal); Formal analysis (equal); Investigation (equal); Methodology (equal); Validation (equal);Visualization (lead); Writing – original draft (lead); Writing – review & editing (equal)

**Pia Dally** - Data curation (equal); Formal analysis (supporting); Investigation (supporting); Methodology (supporting); Validation (equal);Visualization (lead); Writing – review & editing (equal)

**Mirella Al Katrib** - Data curation (equal); Formal analysis (equal); Investigation (equal); Methodology (supporting); Validation (equal);Visualization (lead); Writing – review & editing (equal)

**Mathieu Frégnaux -** Data curation (supporting); Formal analysis (supporting); Investigation (supporting); Methodology (supporting); Validation (supporting); Visualization (supporting); Writing – review & editing (equal)

**Stefania Cacovich -** Formal analysis (supporting); Investigation (supporting); Methodology (supporting); Validation (supporting); Writing – review & editing (equal)

**Frédérique Donsanti** - Formal analysis (supporting); Investigation (supporting); Methodology (supporting); Validation (supporting); Writing – review & editing (equal)

**Armelle Yaïche -** Data curation (equal); Formal analysis (supporting); Investigation (supporting); Methodology (supporting); Validation (equal); Writing – review & editing (equal)

**Karim Medjoubi** - Data curation (equal); Formal analysis (equal); Investigation (supporting); Methodology (equal); Validation (equal); Visualization (equal); Writing – review & editing (equal)

**Thomas Guillemot -** Formal analysis (supporting); Investigation (supporting); Methodology (supporting); Validation (supporting); Writing – review & editing (equal)

**Marion Provost -** Formal analysis (supporting); Investigation (supporting); Methodology (supporting); Validation (supporting); Writing – review & editing (equal)

**Jean Rousset** - Formal analysis (supporting); Investigation (supporting); Methodology (supporting); Project administration (equal); Resources (equal); Validation (supporting); Writing – review & editing (equal)

**Muriel Bouttemy** - Formal analysis (supporting); Investigation (supporting); Methodology (equal); Project administration (equal); Resources (equal); Validation (supporting); Writing – review & editing (equal)

**Nathanaelle Schneider** - Conceptualization (lead); Data curation (supporting); Formal analysis (equal); Funding acquisition (lead); Investigation (lead); Methodology (lead); Project administration (lead); Resources (lead); Validation (lead); Visualization (supporting); Writing – original draft (supporting); Writing – review & editing (lead)

## DATA AVAILABILITY

The data that support the findings of this study are available from the corresponding author upon reasonable request.

## REFERENCES


[1] L. Etgar, P. Gao, Z. Xue, Q. Peng, A.K. Chandiran, B. Liu, Md.K. Nazeeruddin, and M. Grätzel, "Mesoscopic $CH_3NH_3PbI_3/TiO_2$ Heterojunction Solar Cells," J. Am. Chem. Soc. **134**(42), 17396–17399 (2012).
[2] J. Burschka, N. Pellet, S.-J. Moon, R. Humphry-Baker, P. Gao, M.K. Nazeeruddin, and M. Grätzel, "Sequential deposition as a route to high-performance perovskite-sensitized solar cells," Nature **499**(7458), 316–319 (2013).
[3] C. Dong, Z.-K. Wang, and L.-S. Liao, "Progress of Triple Cation Organometal Halide Perovskite Solar Cells," Energy Tech **8**(4), 1900804 (2020).
[4]"Best Research-Cell Efficiency Chart," (n.d.).
[5] S.S. Dipta, and A. Uddin, "Stability Issues of Perovskite Solar Cells: A Critical Review," Energy Technol. **9**(11), 2100560 (2021).
[6] P. Zhang, M. Li, and W.-C. Chen, "A Perspective on Perovskite Solar Cells: Emergence, Progress, and Commercialization," Frontiers in Chemistry **10**, (2022).
[7] P. Schulz, D. Cahen, and A. Kahn, "Halide Perovskites: Is It All about the Interfaces?," Chem. Rev. **119**(5), 3349–3417 (2019).
[8] S.S. Shin, S.J. Lee, and S.I. Seok, "Metal Oxide Charge Transport Layers for Efficient and Stable Perovskite Solar Cells," Adv. Funct. Mater. **29**(47), 1900455 (2019).
[9] P.S.C. Schulze, A.J. Bett, K. Winkler, A. Hinsch, S. Lee, S. Mastroianni, L.E. Mundt, M. Mundus, U. Würfel, S.W. Glunz, M. Hermle, and J.C. Goldschmidt, "Novel Low-Temperature Process for Perovskite Solar Cells with a Mesoporous $TiO_2$ Scaffold," ACS Appl. Mater. Interfaces **9**(36), 30567–30574 (2017).
[10] P. Qin, A.L. Domanski, A.K. Chandiran, R. Berger, H.-J. Butt, M.I. Dar, T. Moehl, N. Tetreault, P. Gao, S. Ahmad, M.K. Nazeeruddin, and M. Grätzel, "Yttrium-substituted nanocrystalline $TiO_2$ photoanodes for perovskite based heterojunction solar cells," Nanoscale **6**(3), 1508–1514 (2014).

[11] X. Feng, K. Shankar, M. Paulose, and C.A. Grimes, “Tantalum-Doped Titanium Dioxide Nanowire Arrays for Dye-Sensitized Solar Cells with High Open-Circuit Voltage,” Angew. Chem. Int. Ed. **48**(43), 8095–8098 (2009).
[12] S. Goetz, D. Mehanni, N. Bansal, B. Kubicek, R.A. Wibowo, M. Bauch, C. Linke, E. Franzke, J. Winkler, T. Meyer, S. Narbey, D. Stock, M. Valtiner, and T. Dimopoulos, “Low-Temperature-Processed Transparent Electrodes Based on Compact and Mesoporous Titanium Oxide Layers for Flexible Perovskite Solar Cells,” ACS Appl. Energy Mater. **5**(5), 5318–5330 (2022).
[13] Y. Numata, R. Ishikawa, Y. Sanehira, A. Kogo, H. Shirai, and T. Miyasaka, “Nb-doped amorphous titanium oxide compact layer for formamidinium-based high efficiency perovskite solar cells by low-temperature fabrication,” J. Mater. Chem. A **6**(20), 9583–9591 (2018).
[14] G. Xiao, C. Shi, K. Lv, C. Ying, and Y. Wang, “Nb-Doping TiO2 Electron Transporting Layer for Efficient Perovskite Solar Cells,” ACS Appl. Energy Mater. **1**(6), 2576–2581 (2018).
[15] Y. Sanehira, N. Shibayama, Y. Numata, M. Ikegami, and T. Miyasaka, “Low-Temperature Synthesized Nb-Doped TiO2 Electron Transport Layer Enabling High-Efficiency Perovskite Solar Cells by Band Alignment Tuning,” ACS Appl. Mater. Interfaces **12**(13), 15175–15182 (2020).
[16] M. Yu, H. Sun, X. Huang, Y. Yan, and W. Zhang, “In Situ-Formed and Low-Temperature-Deposited Nb:TiO2 Compact-Mesoporous Layer for Hysteresis-Less Perovskite Solar Cells with High Performance,” Nanoscale Research Letters **15**(1), 135 (2020).
[17] Y. Lv, B. Cai, Q. Ma, Z. Wang, J. Liu, and W.-H. Zhang, “Highly crystalline Nb-doped TiO2 nanospindles as superior electron transporting materials for high-performance planar structured perovskite solar cells,” RSC Adv. **8**(37), 20982–20989 (2018).
[18] G. Yin, J. Ma, H. Jiang, J. Li, D. Yang, F. Gao, J. Zeng, Z. Liu, and S.F. Liu, “Enhancing Efficiency and Stability of Perovskite Solar Cells through Nb-Doping of $TiO_2$ at Low Temperature,” ACS Appl. Mater. Interfaces **9**(12), 10752–10758 (2017).
[19] B.-X. Chen, H.-S. Rao, W.-G. Li, Y.-F. Xu, H.-Y. Chen, D.-B. Kuang, and C.-Y. Su, “Achieving high-performance planar perovskite solar cell with Nb-doped $TiO_2$ compact layer by enhanced electron injection and efficient charge extraction,” J. Mater. Chem. A **4**(15), 5647–5653 (2016).
[20] M. Abulikemu, M.L. Tietze, S. Waiprasoet, P. Pattanasattayavong, B. E.A. Tabrizi, V. D’Elia, S. Del Gobbo, and G.E. Jabbour, “Microwave-Assisted Non-aqueous and Low-Temperature Synthesis of Titania and Niobium-Doped Titania Nanocrystals and Their Application in Halide Perovskite Solar Cells as Electron Transport Layers,” ACS Omega **7**(8), 6616–6626 (2022).
[21] H.H. Park, “Inorganic Materials by Atomic Layer Deposition for Perovskite Solar Cells,” Nanomaterials **11**(1), 88 (2021).
[22] K. Deng, and L. Li, “Advances in the Application of Atomic Layer Deposition for Organometal Halide Perovskite Solar Cells,” Adv. Mater. Interfaces **3**(21), 1600505 (2016).

[23] Z. Xing, J. Xiao, T. Hu, X. Meng, D. Li, X. Hu, and Y. Chen, "Atomic Layer Deposition of Metal Oxides in Perovskite Solar Cells: Present and Future," Small Methods **4**(12), 2000588 (2020).
[24] V. Zardetto, B.L. Williams, A. Perrotta, F. Di Giacomo, M.A. Verheijen, R. Andriessen, W.M.M. Kessels, and M. Creatore, "Atomic layer deposition for perovskite solar cells: research status, opportunities and challenges," Sustainable Energy Fuels **1**(1), 30–55 (2017).
[25] J.A. Raiford, S.T. Oyakhire, and S.F. Bent, "Applications of atomic layer deposition and chemical vapor deposition for perovskite solar cells," Energy Environ. Sci. **13**(7), 1997–2023 (2020).
[26] W. Zhao, and Y. Duan, "Advanced Applications of Atomic Layer Deposition in Perovskite-Based Solar Cells," Advanced Photonics Research **2**(7), 2100011 (2021).
[27] Y. Yang, Y. Zhang, L. Bai, D.M. Malouangou, J.T. Matondo, J. Pan, S. Dai, M. Cai, X. Liu, and M. Guli, "Research progress of atomic layer deposition technology to improve the long-term stability of perovskite solar cells," J. Mater. Chem. C **10**(3), 819–839 (2022).
[28] Y. Zhang, Y. Yang, M.T. Mbumba, M.W. Akram, E.K. Rop, L. Bai, and M. Guli, "Research Progress of Buffer Layer and Encapsulation Layer Prepared by Atomic Layer Deposition to Improve the Stability of Perovskite Solar Cells," Solar RRL **6**(12), 2200823 (2022).
[29] R.W. Johnson, A. Hultqvist, and S.F. Bent, "A brief review of atomic layer deposition: from fundamentals to applications," Materials Today **17**(5), 236–246 (2014).
[30] Y. Zhao, L. Zhang, J. Liu, K. Adair, F. Zhao, Y. Sun, T. Wu, X. Bi, K. Amine, J. Lu, and X. Sun, "Atomic/molecular layer deposition for energy storage and conversion," Chem. Soc. Rev. **50**(6), 3889–3956 (2021).
[31] A.G. Hufnagel, S. Häringer, M. Beetz, B. Böller, D. Fattakhova-Rohlfing, and T. Bein, "Carbon-templated conductive oxide supports for oxygen evolution catalysis," Nanoscale **11**(30), 14285–14293 (2019).
[32] J.-P. Niemelä, H. Yamauchi, and M. Karppinen, "Conducting Nb-doped TiO2 thin films fabricated with an atomic layer deposition technique," Thin Solid Films **551**, 19–22 (2014).
[33] V. Pore, M. Ritala, M. Leskelä, T. Saukkonen, and M. Järn, "Explosive Crystallization in Atomic Layer Deposited Mixed Titanium Oxides," Crystal Growth & Design **9**(7), 2974–2978 (2009).
[34] G. Luka, L. Wachnicki, R. Jakiela, and E. Lusakowska, "Structural properties and metallic conductivity of Ti 1− x Nb x O 2 films grown by atomic layer deposition on crystalline substrates," J. Phys. D: Appl. Phys. **48**(49), 495305 (2015).
[35] W.J.H. (Willem-J. Berghuis, J. Melskens, B. Macco, S.B. Basuvalingam, M.A. Verheijen, and W.M.M. (Erwin) Kessels, "Atomic layer deposition of Nb-doped TiO2: Dopant incorporation and effect of annealing," Journal of Vacuum Science & Technology A **38**(2), 022408 (2020).
[36] D. Coutancier, S.-T. Zhang, S. Bernardini, O. Fournier, T. Mathieu-Pennober, F. Donsanti, M. Tchernycheva, M. Foldyna, and N. Schneider, "ALD of ZnO:Ti: Growth Mechanism and Application as an Efficient Transparent Conductive Oxide in Silicon Nanowire Solar Cells," ACS Appl. Mater. Interfaces **12**(18), 21036–21044 (2020).

[37] M.V. Khenkin, E.A. Katz, A. Abate, G. Bardizza, J.J. Berry, C. Brabec, F. Brunetti, V. Bulović, Q. Burlingame, A. Di Carlo, R. Cheacharoen, Y.-B. Cheng, A. Colsmann, S. Cros, K. Domanski, M. Dusza, C.J. Fell, S.R. Forrest, Y. Galagan, D. Di Girolamo, M. Grätzel, A. Hagfeldt, E. von Hauff, H. Hoppe, J. Kettle, H. Köbler, M.S. Leite, S. Liu, Y.-L. Loo, J.M. Luther, C.-Q. Ma, M. Madsen, M. Manceau, M. Matheron, M. McGehee, R. Meitzner, M.K. Nazeeruddin, A.F. Nogueira, Ç. Odabaşı, A. Osherov, N.-G. Park, M.O. Reese, F. De Rossi, M. Saliba, U.S. Schubert, H.J. Snaith, S.D. Stranks, W. Tress, P.A. Troshin, V. Turkovic, S. Veenstra, I. Visoly-Fisher, A. Walsh, T. Watson, H. Xie, R. Yıldırım, S.M. Zakeeruddin, K. Zhu, and M. Lira-Cantu, "Consensus statement for stability assessment and reporting for perovskite photovoltaics based on ISOS procedures," Nat Energy **5**(1), 35–49 (2020).
[38] J.W. Elam, and S.M. George, "Growth of ZnO/Al2O3 Alloy Films Using Atomic Layer Deposition Techniques," Chem. Mater. **15**(4), 1020–1028 (2003).
[39] H. Le Tulzo, N. Schneider, D. Lincot, G. Patriarche, and F. Donsanti, "Impact of the sequence of precursor introduction on the growth and properties of atomic layer deposited Al-doped ZnO films," Journal of Vacuum Science & Technology A **36**(4), 041502 (2018).
[40] J. Kruszyńska, J. Ostapko, V. Ozkaya, B. Surucu, O. Szawcow, K. Nikiforow, M. Hołdyński, M.M. Tavakoli, P. Yadav, M. Kot, G.P. Kołodziej, M. Wlazło, S. Satapathi, S. Akin, and D. Prochowicz, "Atomic Layer Engineering of Aluminum-Doped Zinc Oxide Films for Efficient and Stable Perovskite Solar Cells," Advanced Materials Interfaces **9**(17), 2200575 (2022).
[41] D.Y. Lee, J.-H. Park, Y.-H. Kim, M.-H. Lee, and N.-I. Cho, "Effect of Nb doping on morphology, crystal structure, optical band gap energy of TiO2 thin films," Current Applied Physics **14**(3), 421–427 (2014).
[42] R. Khan, H. Ali-Löytty, J. Saari, M. Valden, A. Tukiainen, K. Lahtonen, and N.V. Tkachenko, "Optimization of Photogenerated Charge Carrier Lifetimes in ALD Grown TiO2 for Photonic Applications," Nanomaterials **10**(8), 1567 (2020).
[43] S.B. Basuvalingam, B. Macco, H.C.M. Knoops, J. Melskens, W.M.M. (Erwin) Kessels, and A.A. Bol, "Comparison of thermal and plasma-enhanced atomic layer deposition of niobium oxide thin films," Journal of Vacuum Science & Technology A **36**(4), 041503 (2018).
[44] G.T. Tractz, S.R. Masetto Antunes, G.A. Rodrigues Maia, H. de Santana, M. de Fátima Oliveira, and P.R.P. Rodrigues, "Nb–TiO2/P3HT hybrid solar cell: Oxide production and photovoltaic electrochemical characterization," Optical Materials **121**, 111513 (2021).
[45] Y. Guo, J. Tao, J. Jiang, J. Zhang, J. Yang, S. Chen, and J. Chu, "Low temperature solution deposited niobium oxide films as efficient electron transport layer for planar perovskite solar cell," Solar Energy Materials and Solar Cells **188**, 66–72 (2018).
[46] X. Liu, Y. Xiao, Q. Zeng, J. Jiang, and Y. Li, "Large-Area Organic-Free Perovskite Solar Cells with High Thermal Stability," J. Phys. Chem. Lett. **10**(20), 6382–6388 (2019).
[47] R.D. Chavan, N. Parikh, M.M. Tavakoli, D. Prochowicz, A. Kalam, P. Yadav, P.H. Bhoite, and C.K. Hong, "Mesoscopic TiO2/Nb2O5 Electron Transfer Layer for Efficient and Stable Perovskite Solar Cells," Advanced Materials Interfaces **8**(10), 2100177 (2021).

[48] S.L. Fernandes, A.C. Véron, N.F.A. Neto, F.A. Nüesch, J.H. Dias da Silva, M.A. Zaghete, and C.F. de O. Graeff, "Nb2O5 hole blocking layer for hysteresis-free perovskite solar cells," Materials Letters **181**, 103–107 (2016).
[49] J.A. Christians, P. Schulz, J.S. Tinkham, T.H. Schloemer, S.P. Harvey, B.J. Tremolet de Villers, A. Sellinger, J.J. Berry, and J.M. Luther, "Tailored interfaces of unencapsulated perovskite solar cells for >1,000 hour operational stability," Nat Energy **3**(1), 68–74 (2018).

# FIGURE CAPTIONS

FIG. 7. Mass variations recorded by *in situ* QCM measurements for $TiO_2$ (**a**), $Nb_2O_5$ (**b**) and the three precursor sequences A (**c**), B (**d**), and C (**e**). The pulse times are depicted in colored bands below the curves.

FIG. 8. XPS measurements of the Ti 2p (**a**), Nb 3d (**b**) and N 1s (**c**) peaks of Nb-incorporated $TiO_2$ samples for $n_1$ = 0, 1, 2, 5, 10, 20. The evolution of the Nb doping fraction $x_{Nb}$ calculated from the atomic percentage measured by XPS is depicted with respect to the dopant cycle ratio R (**d**).

FIG. 9. Evolution of the band gap determined by SE with respect to the annealing temperature gathering the data obtained for all tested annealing atmospheres (air, $N_2$, FG). Data is plot depending on the structural properties (amorphous, blue; crystalline, red) with no regard of the Nb doping fraction or the annealing atmosphere conditions.

FIG. 10. J(V) (**a**) and solar cell performance characteristics (PCE, $J_{SC}$, $V_{OC}$ and FF, **b**) of PSC with various ETL compositions. Schematic representation of the complete stack of PSC (**c**).

FIG. 11. Evolution of PCE for both FW and RV measurements at day 0 and day 61 of PSC with bare $TiO_2$ and Nb-$TiO_2$ with $n_1$ = 10, 5 and 1 (**a**). FW and RV J(V) curves for $n_1$ = 1 measured at day 0 and day 61 (**b**).

FIG. 12. Evolution of normalized PV parameters ($J_{SC}$ **a**, $V_{OC}$ **b**, FF **c** and PCE **d**) with time under constant illumination and MPPT of PSC with bare $TiO_2$, bare $Nb_2O_5$ and Nb-$TiO_2$ with $n_1$ = 2, 20. Measurements were done every 15 min; EQE measurements at BOL and EOL (**e**).